



Enhanced photocatalytic conversion of greenhouse gas CO₂ into solar fuels over g-C₃N₄ nanotubes with decorated transparent ZIF-8 nanoclusters



Shengwei Liu ^{a,b,*}, Feng Chen ^b, Sitan Li ^a, Xingxing Peng ^a, Ya Xiong ^a

^a School of Environmental Science and Engineering, Guangdong Provincial Key Laboratory of Environmental Pollution Control and Remediation Technology, Sun Yat-sen University, Guangzhou 510006, PR China

^b State Key Laboratory of Advanced Technology for Material Synthesis and Processing, Wuhan University of Technology, Wuhan 430070, PR China

ARTICLE INFO

Article history:

Received 10 February 2017

Received in revised form 20 March 2017

Accepted 2 April 2017

Available online 6 April 2017

Keywords:

Photocatalyst

CO₂ reduction

g-C₃N₄

Metal-organic frameworks (MOF)

Nanotubes

ABSTRACT

The atmospheric concentration of CO₂ as the dominant greenhouse gas continues to rise and has become a global environmental issue. Photocatalytic CO₂ reduction into solar fuels has been regarded as an ideal solution to reduce CO₂ emissions and to use solar energy. Graphitic carbon nitride (g-C₃N₄) is one of the most promising visible-light-driven photocatalysts for CO₂ reduction. Unfortunately, the CO₂ reduction performance of g-C₃N₄ based photocatalyst is normally limited by the inferior charge separation ability and limited CO₂ adsorption capacity. In this study, two cooperative strategies, that is, combined host nanostructural design and surface guest grafting, are adopted to overcome the aforementioned drawbacks. Specifically, holey graphitic carbon nitride (g-C₃N₄) nanotubes were firstly fabricated to modify the light-harvesting ability, the redox potential as well as the charge separation efficiency. And then, the as-prepared tubular g-C₃N₄ was decorated with suitable amount of transparent zeolitic imidazolate framework-8 (ZIF-8) nanoclusters to further increase CO₂ capture capacity without sacrifice of light absorption capacity. Because of the cooperative effects of nanostructural design and surface grafting, the optimized ZIF-8 modified tubular g-C₃N₄ photocatalysts exhibit a great enhancement in photocatalytic CH₃OH production efficiency by more than 3 times, relative to the bulk g-C₃N₄ (BCN) photocatalyst synthesized by conventional pyrolysis of melamine. This work will enlighten a promising strategy to construct efficient photocatalyst for greenhouse gas CO₂ resourcing, by taking advantage of the cooperative effects of semiconductor nanostructures and surface metal-organic framework grafters.

© 2017 Elsevier B.V. All rights reserved.

1. Introduction

The continuing increase of atmospheric CO₂ emissions is causing global concerns of greenhouse effect. Reducing CO₂ emissions by CO₂ capture, storage and utilization attracted worldwide interest. In particular, artificial photosynthesis involving the photocatalytic conversion of CO₂ into solar fuels is regarded as one of the most promising strategy for CO₂ utilization. The artificial photosynthesis is not only a feasible method to eliminate CO₂ emission and to reduce the threat of greenhouse effect to global climate, but it is also a reliable solution to achieve CO₂ resourcing and to convert solar energy to storable and transportable chemical energy with

high energy density [1–5]. Since the first report of semiconductor mediated photocatalytic CO₂ reduction by Inoue and co-workers [6], a variety of semiconductor photocatalysts, including TiO₂, ZnO, CdS, GaP and SiC, had been intensively studied for enhanced photocatalytic reduction of CO₂ to valuable chemicals [7–12]. Recently, graphitic carbon nitride (g-C₃N₄) as a stable and nontoxic organic semiconductor attracted great attentions and was introduced for diverse photocatalytic applications, including photocatalytic CO₂ reduction [13–18]. Relative to conventional inorganic semiconductor photocatalysts like TiO₂, g-C₃N₄ possesses suitable band structure (band gap, ca. 2.7 eV; energy potential of conduction band (CB), ca. –1.1 V vs. NHE; energy potential of valence band (VB), ca. 1.6 V vs. NHE) with desirable visible-light response and suitable photocatalytic redox potential for triggering reactions of CO₂ reduction and water oxidation. Moreover, g-C₃N₄ based photocatalysts are generally of low-cost and exhibit excellent chemical/thermal stability [19].

* Corresponding author at: School of Environmental Science and Engineering, Guangdong Provincial Key Laboratory of Environmental Pollution Control and Remediation Technology, Sun Yat-sen University, Guangzhou 510006, PR China.

E-mail address: liushw6@mail.sysu.edu.cn (S. Liu).

Nevertheless, the photocatalytic CO₂ reduction performance of available g-C₃N₄ photocatalysts was usually still far from satisfying. Conventional bulk g-C₃N₄ photocatalysts were normally produced by pyrolysis of cost-effective precursors such as melamine, urea, cyanamide and thiourea. The as-prepared g-C₃N₄ was generally characteristic of low specific surface area and low CO₂ capture capacity. Meanwhile, the recombination rate of photogenerated electrons and holes within bulk g-C₃N₄ was relatively high, which severely impair the apparent photocatalytic activity [1]. In this regard, many strategies have been thus devised to enhance photocatalytic CO₂ reduction performance of g-C₃N₄ photocatalysts. Among the diverse methods, subtle nanostructural design seems simple and feasible. So far, g-C₃N₄ with various nanostructures, such as mesoporous structures [20,21], nanosheets [22–25], nanowires [26,27] and nanocomposites [28–30], had been successfully synthesized for enhanced photocatalytic CO₂ reduction. In most case, the g-C₃N₄ nanostructures have tunable band structure and more or less higher specific surface area relative to the bulk counterpart. So, the light absorption ability, the charge separation efficiency and the CO₂ capture capacity of g-C₃N₄ nanostructures can be modified to some extent, leading to better photocatalytic CO₂ reduction performance. Even though, modification of g-C₃N₄ nanostructures with other cooperative functional moieties seems necessary in order to further enhance the photocatalytic CO₂ reduction performance. In fact, coupling g-C₃N₄ nanostructures with other semiconductors with suitable band edge positions was frequently adopted to further promote the spatial separation of photoexcited electrons and holes [31]. However, fewer efforts have been devoted to the decoration of g-C₃N₄ with suitable adsorbents as adsorption antenna to further enhance CO₂ capture, which is actually the prerequisite for CO₂ activation and following photocatalytic reduction reactions. Several adsorbents, like graphene, activated carbon, zeolites and some mesoporous materials, have been used to combine with certain photocatalysts for enhancing CO₂ reduction. Unfortunately, the improvements were often quite limited. The employed adsorbents usually brought some side effects, for example, the light shielding, trapping photogenerated charges, occupying redox active sites, nonselective adsorption towards reactants and products, etc.

Metal-organic frameworks (MOFs), a novel class of porous materials constructed by metal-containing clusters and organic ligands, attracted growing research interests owing to their potential applications in diverse fields, in particular, adsorption and catalysis. Some MOF materials even exhibited semiconductor behavior and can be directly employed as photocatalyst for CO₂ reduction, although the efficiency was rather low. More importantly, a variety of MOF materials exhibited exiting potential for high-capacity CO₂ capture [32]. Therefore, it is supposed that combining the MOF materials with semiconductor photocatalyst would largely enhance the CO₂ capture and thus promote the overall photocatalytic CO₂ reduction efficiency. Zeolitic imidazolate framework-8 (ZIF-8), a typical member of the MOF family, constructed by zinc ions and imidazolate linkers, has been widely studied due to its permanent porosity, excellent thermal/chemical stability, good water tolerance and CO₂ affinity [33]. Besides, two additional characteristics of ZIF-8 make it an excellent candidate for constructing ZIF-8/semiconductor composites for photocatalytic CO₂ reduction. One trait is related to the transparency of ZIF-8 [34]. In this way, the incorporation of ZIF-8 within the semiconductor matrix will not impair too much the light harvesting capacity. Another trait is related to the adsorption selectivity within ZIF-8 [35–37]. It is very important for the photocatalytic CO₂ reduction reaction that the photocatalytic system can absorb the reactant CO₂ efficiently but not being affinitive to the reduction products, like CH₄, CH₃OH etc. This adsorption selectivity is essential for inhibiting the back reactions of hydrocarbon products and, for inhibiting

the photocatalyst deactivation associated with the possible surface carbon deposition during the photocatalytic CO₂ reduction reaction. In this regard, as an example, ZIF-8 nanoclusters were introduced to decorate the well-designed g-C₃N₄ nanotubes in this study, demonstrating their cooperative effects in enhancing photocatalytic CO₂ reduction performance. A time-saving and low temperature synthesis protocol was developed to prepare the holey g-C₃N₄ nanotubes at first, which was then decorated with ZIF-8 nanoclusters by heterogeneous deposition. Because of the cooperative effects of nanostructural design and surface grafting, the optimized g-C₃N₄/ZIF-8 photocatalysts presented improved light-harvesting ability, increased charge separation efficiency and elevated CO₂ adsorption capacity, and consequently, exhibiting a great enhancement in photocatalytic CH₃OH production efficiency by more than 3 times, relative to the bulk g-C₃N₄ (BCN) photocatalyst synthesized by conventional pyrolysis of melamine.

2. Experimental section

2.1. Preparations of photocatalysts

2.1.1. Fabrication of holey g-C₃N₄ nanotubes

The holey g-C₃N₄ nanotubes (named as TCN) were prepared according to a published literature with some modification [38]. In a typical synthesis process, 0.52 g of melamine was dissolved in 20 mL of ethylene glycol to make a saturated solution. And then 60 mL of 0.12 M nitric acid aqueous solution was added into the above solution dropwise under stirring. After stirring for 10 min, the generated white precipitation was collected and washed with ethanol for three times, and then dried at 55 °C in a vacuum oven for 8 h. The obtained white products were annealed at 350 °C for 1 h with a heating rate of 8 °C min⁻¹, to get the final TCN. For comparison, Bulk g-C₃N₄ (named as BCN) was also synthesized by pyrolysis of melamine at 550 °C for 2 h [39].

2.1.2. Fabrication of g-C₃N₄/ZIF-8 composite

The fabrication of g-C₃N₄/ZIF-8 composite was conducted by simple in-situ heterogeneous deposition method. In brief, 100 mg of the as-prepared g-C₃N₄ nanotubes powder was dispersed into 30 mL methanol under ultrasonic irradiation for 15 min to obtain a uniform suspension. Subsequently, a certain amount of zinc acetate hexahydrate and 2-methylimidazole was added into the above suspension, successively (the mole ratio of zinc acetate hexahydrate and 2-methylimidazole was 1:4). After stirred for 1 h, the suspension was aged at room temperature for another 24 h ensuring that the ZIF-8 nanoclusters uniformly grown on the surface of g-C₃N₄ nanotubes. Finally, the precipitation was collected by centrifugation and washed with water for three times, and then dried at 80 °C for 12 h. The obtained samples were denoted as TCNZx (x is related to the initially designed mass ratio of g-C₃N₄ to ZIF-8) and listed in Table 2.

2.1.3. Fabrication of ZIF-8 nanocrystals

ZIF-8 nanocrystals were synthesized following the previously reported procedures [40]. Typically, 2 mmol zinc acetate hexahydrate and 8 mmol 2-methylimidazole were dissolved in 40 mL methanol successively and stirring for 3 h. The white powder product was separated from the milky colloidal dispersion by centrifugation after aging at room temperature for 24 h. And then, the product was washed with methanol for three times and dried at 80 °C for 12 h. The obtained sample was named as p-Z.

2.2. Characterizations of photocatalyst

The prepared products were characterized by different analytical techniques. The crystallographic phase of these obtained

products was determined by powder X-ray diffraction (XRD) using a D/Max-RB X-ray diffractometer (Rigaku, Japan) with Cu $K\alpha$ irradiation at a scanning rate of $0.05^\circ 2\theta \text{ s}^{-1}$. Field-emission scanning electron microscopy (a JEOL JSM-7500F microscope, Japan) linked with an Oxford Instruments X-ray analysis system together with Transmission electron microscopy (a JEOL JEM-2100F microscope, Japan) were used to examine the microstructures and components of the as-prepared samples. X-ray photoelectron spectroscopy (XPS) measurements were performed on an ultrahigh vacuum VG ESCALAB 210 electron spectrometer (monochromated Al $K\alpha$ source). All the binding energies were calibrated using the C 1s peak at 284.8 eV. The CHNS elemental analyzer (Vario EL cube, Elementar Analysensysteme GmbH, Germany), equipped with a balance which is accurate up to one over one million, was used to analyze the content of C and N. Thermogravimetric analysis was performed in air using a DTG-60H analyzer (Shimadzu, Japan) from room temperature to 800°C with a heating rate of $10^\circ\text{C min}^{-1}$. Nitrogen adsorption-desorption isotherms were measured on an ASAP 2020 gas adsorption apparatus (Micromeritics Instrument, USA). All the samples were degassed at 180°C prior to nitrogen sorption measurements. The pore size distributions were determined using the adsorption data according to the Barrett–Joyner–Halenda (BJH) method. The Brunauer–Emmett–Teller surface area (S_{BET}) was determined by a multipoint BET method using adsorption data in the relative pressure (P/P_0) range of 0.05–0.3. The volume of nitrogen adsorbed at the relative pressure (P/P_0) of 0.97 was used to determine the pore volume and the average pore size. The CO₂ adsorption measurement was carried out under ambient temperature using a TriStar II 3020 carbon dioxide adsorption apparatus (Micromeritics, USA). All the samples were degassed at 150°C for 4 h before CO₂ adsorption measurement. The optical properties were analyzed by diffuse reflectance spectroscopy (DRS) on a UV-vis spectrophotometer (UV-2550, SHIMADZU, Japan), with BaSO₄ as the reflectance standard. Photoluminescence (PL) spectra were obtained on a Fluorescence spectrophotometer (F-7000, Hitachi, Japan) at room temperature. The Photo Multiplier Tube voltage was 700 V, the scanning speed was 1200 nm/min, and the excitation wavelength was 350 nm. The slit width used for the excitation and emission were both 1.0 nm. Fourier transform infrared (FTIR) spectra were recorded on an IR Affinity-1 FTIR spectrometer (Shimadzu, Japan). The zeta potentials of typical samples were performed on a zeta potential analyzer at room temperature (Malvern, Zetasizer Nano, ZS90). Before the measurement, 5 mg of each sample powder was dispersed in deionized water (100 mL) by ultrasonication for 15 min. The zeta potential of each sample was tested for three times by testing the suspension with the initial pH value.

2.3. Examination of photocatalytic CO₂ reduction performance

The evaluation of gas-phase based photocatalytic CO₂ reduction activity was carried out in a 200 mL self-made Pyrex reactor at atmospheric pressure and room temperature. The reactor has two openings which were sealed using a silicone rubber septum. In a typical photocatalytic experiment, 100 mg of as-prepared photocatalyst sample was dispersed into 10 mL distilled water in the glass reactor under ultrasonic irradiation for ca. 30 min. Afterward, the reactor was kept at 80°C for 2 h for water evaporation, and finally, the sample was deposited on the bottom of the reactor as uniform thin film. Before irradiation, the reactor was blown with nitrogen for 30 min to remove air, and to ensure that the reaction system was under anaerobic conditions. CO₂ and H₂O vapor were generated by *in situ* reaction of NaHCO₃ (84 mg, put into the reactor before seal) and H₂SO₄ aqueous solution (0.3 mL, 2 M, introduced into the reactor using a syringe). A 300 W full-spectrum Xe lamp was served as the light source and positioned 10 cm away from the photocat-

alytic reactor. After light irradiation for 1 h, 1 mL of evolved gas product was extracted from the reactor, which was then detected by a gas chromatograph (GC-2014C, Shimadzu, Japan) equipped with a flame ionized detector (FID). Products were calibrated with a standard gas and determined by the retention time. The carrier gas used in the GC-2014C was high purity nitrogen.

2.4. Photoelectrochemical measurements

The transient photocurrent analyses and Mott–Schottky plots were obtained on an electrochemical analyzer (CHI660C electrochemical workstation, Chenhua Instrument, Shanghai, China) in a standard three-electrode configuration including a working electrode, a counter electrode and a reference electrode. The as-prepared samples serve as the working electrodes with an active area of *ca.* 0.5 cm², a platinum wire serves as the counter electrode and Ag/AgCl (saturated KCl) act as the reference electrode. A 3 W LED ($\lambda = 365 \text{ nm}$) lamp with a focused intensity of 80.0 mW cm^{-2} was utilized as light source. A 0.5 M Na₂SO₄ aqueous solution was used as the electrolyte. Working electrodes were prepared as follows: 0.1 g of the as-obtained photocatalyst was ground together with 2.0 mL of ethanol to form slurry. Afterward, the slurry was coated onto a 2 cm × 1.5 cm F-doped SnO₂-coated glass (FTO glass) electrode by doctor blade method. The electrodes were then dried at 80°C in an oven. All of the used working electrodes had a similar film thickness ($\sim 15 \mu\text{m}$). Mott–Schottky plots were recorded by using the Impedance–Potential mode. The Mott–Schottky plots were obtained in darkness at a fixed frequency of 1.0, 2.0, and 3.0 kHz. The potential ranged from -1.0 to 1.0 V (vs Ag/AgCl) with a scanning rate 50 mV/s .

2.5. The *in situ* FTIR measurements

The *in situ* FTIR spectra were obtained through an *in situ* diffuse reflectance Fourier transform infrared spectrometer (Nicolet iS50, TMO, US). The sample was degassed for 4 h at 150°C prior to measurement. Then the degassed sample was sealed in specimen chamber and purged with nitrogen for one hour to remove air. After that, a mixed gas of CO₂ and water vapour was flowed into the specimen chamber for another hour. Subsequently, the sample was irradiated with a LED lamp (365 nm) for two hours and the infrared absorbance was recorded simultaneously.

3. Results and discussion

3.1. Microstructures and components

The X-ray diffraction was performed to investigate the crystal structure of the as-prepared various samples and the results were shown in Fig. 1. Two distinctive XRD peaks were observed for sample TCN and BCN, characteristic of a graphite-like structure. The strong diffraction peak of sample TCN was located at about 27.4° ($d = 0.326 \text{ nm}$), which was close to that of sample BCN. This strong diffraction peak was related to the interplanar stacking of conjugated aromatic systems, corresponding to the (002) plane of g-C₃N₄ [41]. Notably, the small diffraction peak was located at about 17.4° ($d = 0.49 \text{ nm}$) for sample TCN, which was very different from that for sample BCN, locating at about 13° ($d = 0.681 \text{ nm}$). The small diffraction peak could be related to the in-plane repeating unit. It was suggested that sample TCN was constructed by the *s*-triazine based building units, while the sample BCN was built by the tri-*s*-triazine based repeating units [31,38]. The variation in basic building blocks for sample TCN versus sample BCN would result in their different band structures.

The surface grafting of ZIF-8 nanoclusters on g-C₃N₄ nanotubes did not affect the crystal structure too much. The two characteris-

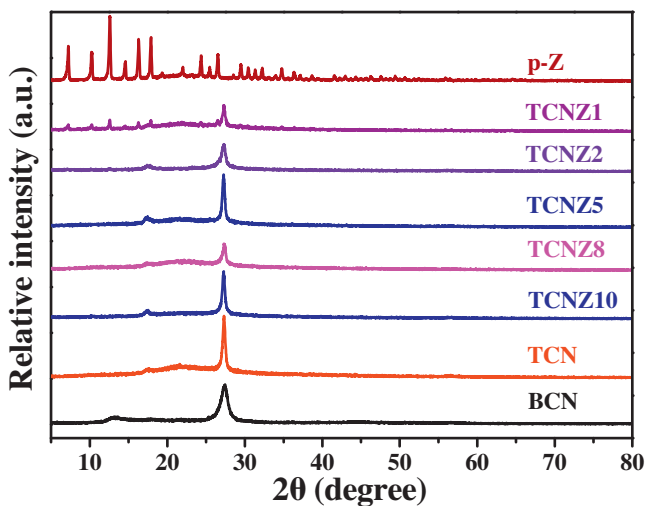


Fig. 1. XRD patterns of the as-synthesized various samples.

tic XRD peaks were remained for all the TCNZx samples. The XRD pattern of the as-synthesized pure ZIF-8 nanocrystals (sample p-Z) matched well with the published patterns [41,42]. Note that, the as-prepared g-C₃N₄ nanotubes are negatively charged (Fig. S1 in the Supporting information) and thus have good affinity to zinc ions. Therefore, ZIF-8 nanoclusters can grow on the surface of g-C₃N₄ nanotubes without any additional surface modification. However, the grafted ZIF-8 nanoclusters on g-C₃N₄ nanotubes for most TCNZx samples did not exhibited obvious characteristic XRD peaks of the ZIF-8, until the content of grafted ZIF-8 was high enough. In the present study, several clear XRD peaks assigned to ZIF-8 was detected when the initially designed mass ratio of ZIF-8 to g-C₃N₄ was 1 (sample TCNZ1).

The morphology and microstructures of the as-prepared pure g-C₃N₄ nanotubes (TCN) and the typical ZIF-8 grafted g-C₃N₄ nanotubes (TCNZ8) were investigated using field-emission scanning electron microscopy (FESEM) and transmission electron microscopy (TEM). The results were show in Fig. 2. As can be clearly seen from Fig. 2a and b, the as-prepared pure g-C₃N₄ nanotubes was mainly composed of porous nanotubes with numerous holes

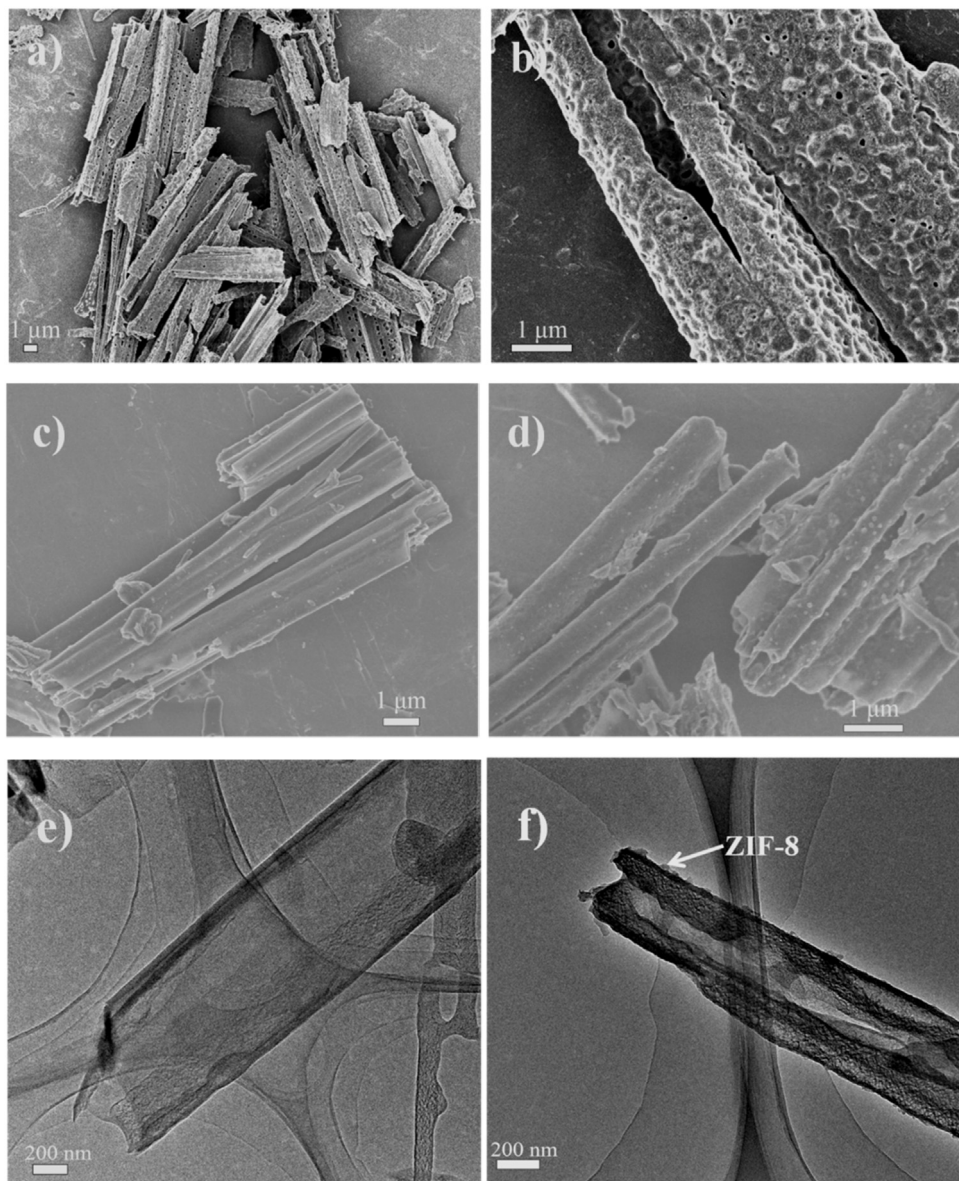


Fig. 2. FESEM (a-d) and TEM images (e, f) for the sample TCN (a, b and e) and sample TCNZ8 (c, d and f).

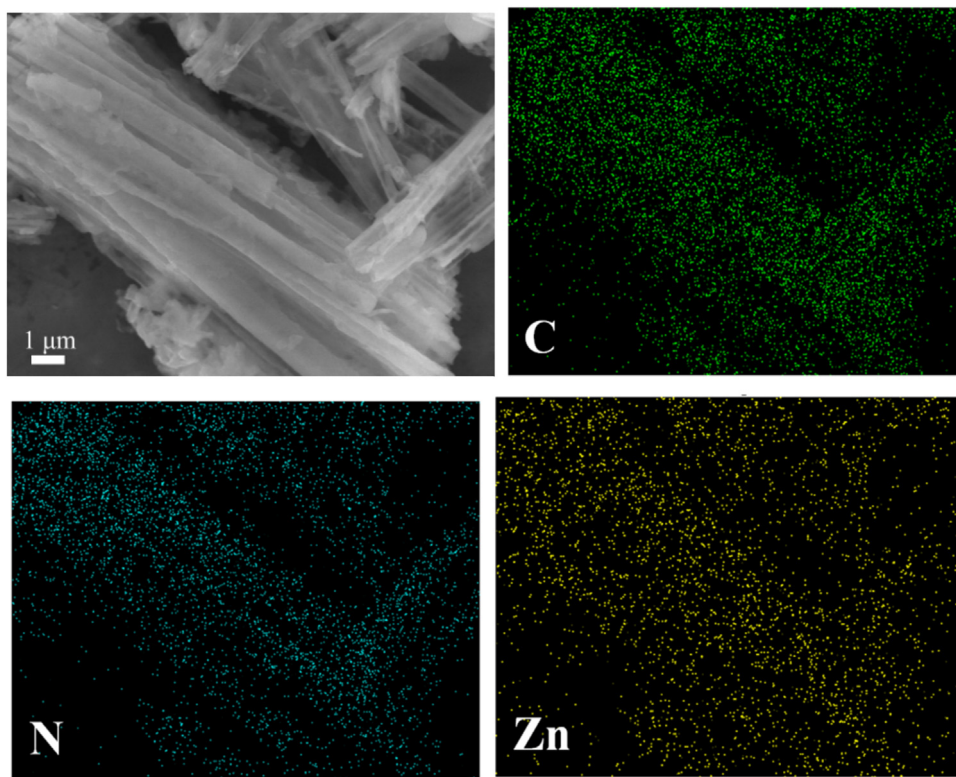


Fig. 3. EDX elemental mapping of the typical sample TCNZ1.

on the surface. Overall, these $\text{g-C}_3\text{N}_4$ nanotubes were not uniform in length and diameter, having diameters of 0.5–3 μm and lengths of several tens to hundreds micrometers. Relatively, the thicknesses of the tube walls are thin and are comparable to each other, of several tens nanometers. The corresponding TEM image (Fig. 2e) further confirmed the tubular morphology with penetrated holes across the tube wall. The unique texture of these $\text{g-C}_3\text{N}_4$ nanotubes shall endow them with several benefits for photocatalytic CO_2 reduction reaction. It has been well documented that the thin tubular structures favor charge separations [43–45]. Meanwhile, the tubular morphology and the holes penetrating the tube wall shall facilitate the mass transportation of reactants and products during photocatalytic reactions. After deposition of suitable amount of ZIF-8 nanoclusters on the $\text{g-C}_3\text{N}_4$ nanotubes (sample TCNZ8), it is obvious that the overall tubular morphology was remained (Fig. 2c, d and f). Notably, most of the pores on the tube wall were filled and the surface of the modified $\text{g-C}_3\text{N}_4$ nanotubes turned to be relatively smoother (Fig. 2c and d). In addition, some protruded nanoparticles were observed on tube wall of $\text{g-C}_3\text{N}_4$ nanotubes. Both aspects suggested that the ZIF-8 was successfully grafted on the surface of the $\text{g-C}_3\text{N}_4$ nanotubes, which was further confirmed by the corresponding TEM image in Fig. 2f. The thickness of the tube wall was obviously increased after ZIF-8 deposition and, some ZIF-8 nanoclusters were protruded out. Moreover, the Energy-dispersive X-ray spectroscopy (EDS) elemental mapping of the ZIF-8 modified $\text{g-C}_3\text{N}_4$ nanotubes (Fig. 3) clearly indicated that Zn element was indeed distributed homogeneously along the nanotubes, in addition to C and N elements.

Thermogravimetric (TG) analysis (Fig. 4) was carried out in air to determine the actual loading contents of deposited ZIF-8 in the final TCNZx products. All the three tested samples demonstrated good thermal stability against phase transformation below 350 °C. A total weight loss of about 65% was recorded for pure ZIF-8 from approximately 350 °C–620 °C, corresponding to the decomposition of the metal organic framework to produce thermal-stable ZnO ,

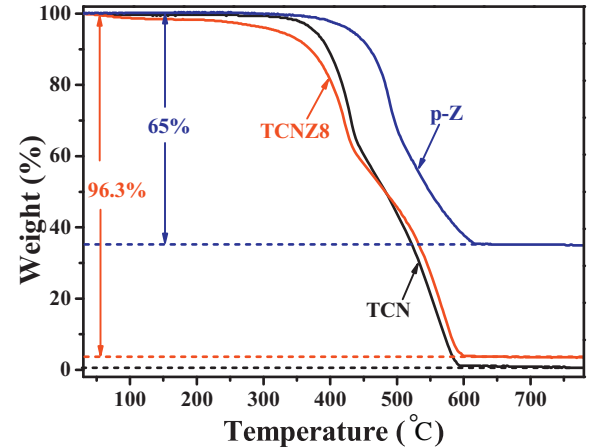


Fig. 4. TG analyses of sample p-Z, TCN and TCNZ8.

which was in agreement with the calculated weight loss of 64%. The pure $\text{g-C}_3\text{N}_4$ nanotubes (sample TCN) presented a weight loss of 100% in the temperature range from 400 to 600 °C, associated with the complete sublimation and/or decomposition of $\text{g-C}_3\text{N}_4$. The TG curves of the ZIF-8 modified $\text{g-C}_3\text{N}_4$ nanotubes (sample TCNZ8) show similar trend to that of the sample TCN. But the weight loss for TCNZ8 was about 96.3% in the similar temperature range, which was less than that for sample TCN. The remaining mass was related to the residual ZnO derived from surface deposited ZIF-8 on sample TCNZ8. The chemical composition of ZIF-8 can be indexed as $\text{Zn}(\text{2-methylimidazole})_2$ with a molecular mass of 227.6 g/mol, and each structural unit contains one Zn (65.4 g/mol). Owing to a variation in mass loss of about 3.7% for TCNZ8 versus TCN, the actual loading content of surface deposited ZIF-8 on sample TCNZ8 could be calculated to be 10.3%. It was understandable that the actual

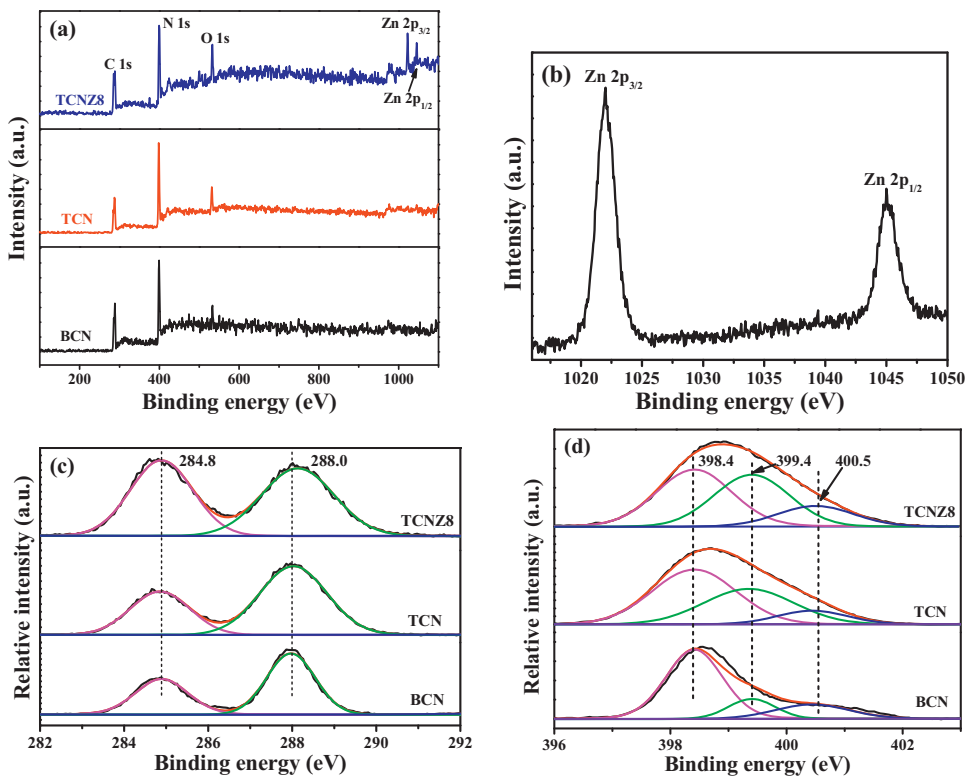


Fig. 5. (a) XPS survey spectra of the sample BCN, TCN and TCNZ8 and the corresponding high resolution XPS spectra of (b) Zn 2p for sample TCNZ8, (c) C 1s and (d) N 1s for sample BCN, CNT and TCNZ8.

amount of surface deposited ZIF-8 on g-C₃N₄ tubes was somewhat less than the designed value.

The X-ray photoelectron spectroscopy (XPS) was investigated to further analyze the variation in chemical compositions and states of typical samples, and the results were shown in Fig. 5. All the XPS survey spectra (Fig. 5a) for sample BCN, TCN, and TCNZ8 clearly reflected the XPS peaks assigned to C 1s, N 1s, and O 1s. The O 1s signal probably came from the absorbed CO₂ and H₂O on the surface of the samples. Notably, as expected, Zn 2p was also presented in the XPS survey spectrum for sample TCNZ8. The high-resolution XPS spectra of Zn 2p were displayed in Fig. 5b, with two peaks locating at 1022.0 eV and 1044.9 eV, corresponding to Zn 2p_{3/2} and Zn 2p_{1/2}, respectively [46,47]. Although it was difficult to distinguish the oxidation states of Zn by only using Zn 2p spectra due to the overlap of binding energy range of Zn⁰ and Zn²⁺, the chemical states of Zn shall be Zn²⁺, taking account of the non-reducing synthesis condition and previous study by Zn LMM Auger spectra [46].

The C 1s spectra for sample BCN, TCN and TCNZ8 can be fitted into two peaks, centered at 284.8 and 288.0 eV (Fig. 5c), which were ascribed to sp² C-C bonds and sp²-hybridized carbon of N=C-N coordination, respectively [13,48]. The peak area of the former peak becomes large because of the existence of 2-methylimidazole after surface modification. The N 1s spectra for sample BCN, TCN and TCNZ8 can be deconvoluted into three peaks (Fig. 5d). The first peak belongs to sp²-hybridized aromatic nitrogen atoms bonded to carbon atoms (C=N-C). The second peak is ascribed to the tertiary N-(C)₃ groups. The third peak can be assigned to the N bonded with H atoms (N-H) [48–50]. The peak area ratio of N-(C)₃ to C=N-C is increased after nanostructuring and is further increased after the additional ZIF-8 grafting. Overall, the chemical states of carbon are similar for BCN, TCN and TCNZ8, but there are changes in the chemical states of nitrogen for the three samples. Quantitative analysis from XPS revealed that the C/N atomic ratio of TCN (0.57) is much smaller than that of BCN (0.69). Elemental analysis by the CHNS ele-

Table 1

The element content of C and N for sample BCN and TCN by the CHNS elemental analyzer.

| Sample | C (%) | N (%) | C:N |
|--------|-------|-------|------|
| BCN | 34.91 | 62.74 | 0.65 |
| TCN | 31.08 | 65.50 | 0.55 |

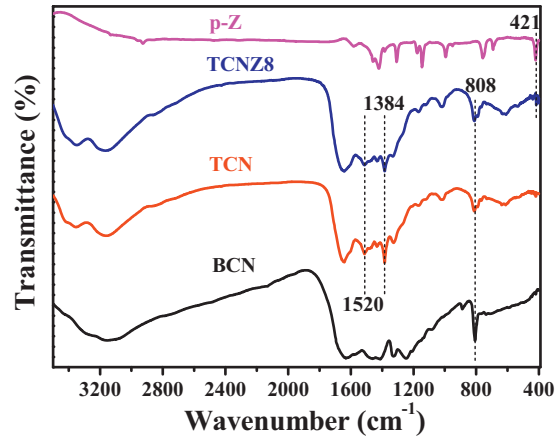


Fig. 6. FTIR spectra of the as-synthesized typical samples: sample BCN, TCN, TCNZ8 and p-Z.

mental analyzer (Table 1) also reflected that the TCN has a smaller C/N atomic ratio (0.55) than that of BCN (0.65), indicating that the TCN is nitrogen-rich graphitic carbon nitride.

The Fourier transform infrared (FTIR) spectra of the as-synthesized typical samples were shown in Fig. 6. Basically, the sample BCN, TCN and TCNZ8 share the similar IR vibrational modes, suggesting that the basic structural framework was not damaged

Table 2

Comparison of the S_{BET} , pore volume, average pore size, CO_2 adsorption and CH_3OH production rate for the as-prepared samples.

| Sample | S_{BET} (m^2/g) | Pore volume (cm^3/g) | Average pore size (nm) | CO_2 adsorption (mmol/g) | CH_3OH production rate ($\mu\text{mol}/(\text{h}\cdot\text{g})$) |
|--------|--|--|------------------------|-----------------------------------|--|
| BCN | 9 | 0.04 | 17 | 0.019 | 0.24 |
| TCN | 11 | 0.02 | 7.5 | 0.029 | 0.49 |
| TCNZ10 | 17 | 0.035 | 8.5 | 0.038 | 0.64 |
| TCNZ8 | 19 | 0.032 | 7.0 | 0.040 | 0.75 |
| TCNZ5 | 20 | 0.04 | 8.5 | 0.041 | 0.45 |
| TCNZ2 | 23 | 0.026 | 4.5 | 0.049 | 0.31 |
| TCNZ1 | 173 | 0.1 | 2.4 | 0.135 | 0.16 |
| p-Z | 1345 | 0.66 | 1.9 | 0.863 | 0 |

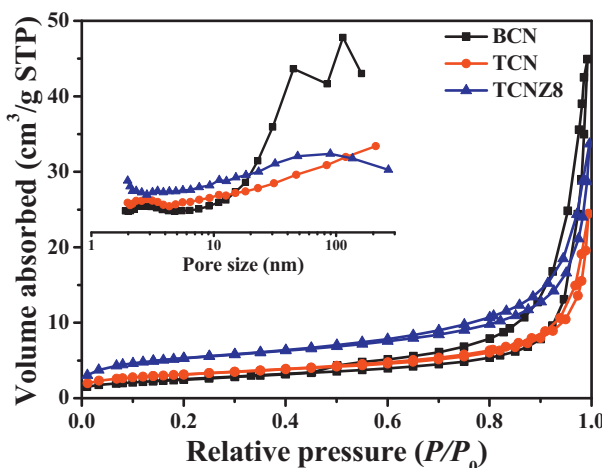


Fig. 7. N_2 sorption isotherms and the corresponding pore size distribution curves (inset) of sample BCN, TCN and TCNZ8.

by either nanostructural design or surface modification. The broad peaks in the range of 3000–3500 cm^{-1} were attributed to the stretching vibration modes of NH and NH₂ groups [51,52]. The peaks between 1000 and 1650 cm^{-1} were typical stretching modes of C–N heterocycles [53]. Note that, the peak at around 1384 and 1520 cm^{-1} in the spectra of holey g-C₃N₄ nanotube were corresponded to the vibration band of nitrate moiety and the band of protonated amine, respectively [38]. The adsorption peak appears at about 808 cm^{-1} was the characteristic breathing mode of the triazine unit [54,55]. Overall, the IR results confirm that the present holey C₃N₄ nanotube as well as the ZIF-8 modified counterpart was graphitic phase, consistent with the XRD result. Moreover, a new band emerged at approximately 421 cm^{-1} for the sample TCNZ8, which was assigned to the Zn–N stretching mode [56], suggesting the existence of ZIF-8 in the composite.

3.2. Adsorption properties

The N₂ sorption measurements are used to investigate the pore structure and specific surface area of as-synthesized samples. As shown in Fig. 7, all the adsorption-desorption isotherms of BCN, TCN and TCNZ8 are of type IV classification [57–59]. At high relative pressures, the isotherms exhibited hysteresis loop associated with capillary condensation of gases within mesopores. The hysteresis loop covers relatively wide range of relative pressures, suggesting the wide mesopore size distributions, which is confirmed by the corresponding broad BJH pore-size distributions (inset in Fig. 7). In particular, in the relative pressure (P/P_0) range from 0.9 to 1.0, the sample BCN exhibit relatively high adsorption, consistent with the existence of a large portion of larger mesopores and macropores. It was reported that those larger mesopores and macropores was mainly associated with inter-particle aggregations [13]. In comparison with sample BCN, the adsorption at the high relative

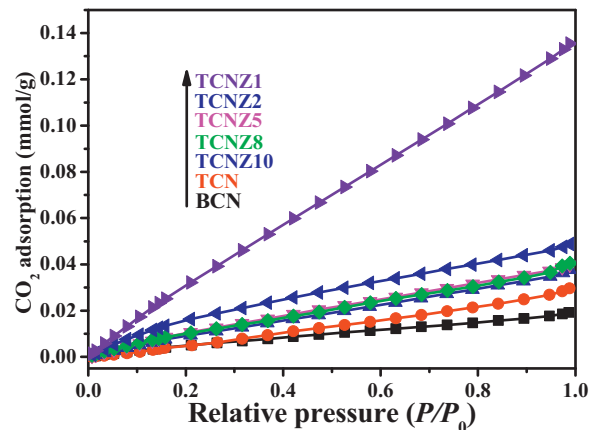


Fig. 8. CO_2 adsorption curves of the sample BCN, TCN and TCN/ZIF-8 composite.

pressures was much less for sample TCN and TCNZ8. Some of the larger mesopores and macropores were diminished. In contrast, the portion of smaller mesopores, associated with intra-aggregation, was increased to great extent by textural modification (sample TCN) and/or surface modifications (TCNZ8). The specific surface area, pore volume, and average pore size of all samples are summarized in Table 2. Overall, in the present study, by constructing tubular nanostructures of g-C₃N₄, the specific surface area can be increased, and more small-sized mesopores are generated, but the overall pore volume is somewhat less than that of the bulk g-C₃N₄. Moreover, combined textural modification with surface guest modification, the specific surface area can be further increased, and even more small-sized mesopores are generated.

It has been well documented that the adsorption of CO₂ onto the photocatalyst surface was the first essential step affecting the reaction pathway and dynamics of the photocatalytic CO₂ reduction [2]. The CO₂ adsorption performance of samples BCN, TCN and TCNZx was investigated using CO₂ adsorption isotherms (Fig. 8). Essentially, all the studied samples show linear relationship between CO₂ adsorption capacity and relative pressure in the relative pressure (P/P_0) range of 0.1–1.0. Such relationship suggests the dominant physical interaction between CO₂ and the studied samples [60]. Note that, in the low relative pressure region ($P/P_0 < 0.1$), a relative fast increase in CO₂ uptake occurred, indicating the initial chemical adsorption of CO₂ on the whole studied samples [34]. The sample TCN has higher specific surface area, and consequently, the sample TCN samples are more effective in CO₂ adsorption. Moreover, with the incorporation of ZIF-8, the CO₂ adsorption capacity of TCNZx samples was further improved. With increasing the introduced ZIF-8, the CO₂ adsorption capacity of TCN was steadily increased. Therefore, a combined textural modification and surface guest modification is efficient in tuning the adsorption property of g-C₃N₄ photocatalyst.

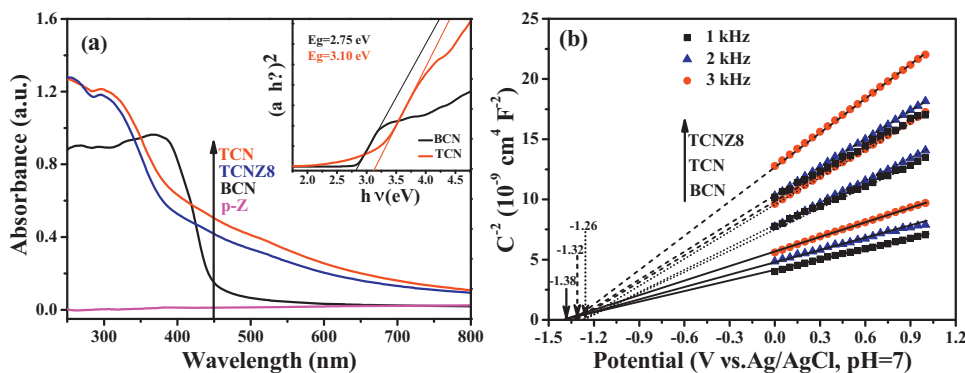


Fig. 9. (a) UV-vis diffuse reflectance of the typical samples and the estimated band gap energies for sample TCN versus BCN (inset); (b) Mott-Schottky plots collected at different frequency of typical samples.

3.3. Optical and electronical properties

The UV-vis diffuse reflectance spectroscopy (DRS) was measured to study the optical properties and electronic structure of the as-prepared samples. First of all, the electronic structure of $\text{g-C}_3\text{N}_4$ can be altered to great extent by nanostructural design. And consequently, two aspects of significant changes in optical properties occurred. As shown in Fig. 9a, compared with BCN, the adsorption edge of TCN is blue shifted from about 450 to 400 nm. Accordingly, the bandgap of TCN was calculated to be 3.10 eV, as compared to 2.75 eV for BCN (inset in Fig. 9). This may be ascribed to quantum confinement effects [52,61]. Furthermore, relative to sample BCN, a very strong absorption tail in the broad range of 450–800 nm is clearly presented for sample TCN. The increased visible light absorption shall be beneficial for the overall apparent photocatalytic performance. The long-tail absorption in the visible light region is probably associated with abundant surface defects in sample TCN. Such a statement is in agreement with the great deviation in C/N ratio for sample TCN based on XPS results.

ZIF-8 is usually transparent, having nearly no light absorption in the UV and visible light range [62], which is consistent with the present result for the as-prepared ZIF-8 crystals. As a consequence, after surface ZIF-8 deposition, very slight variation in the light absorption capacity is observed for TCNZ8 versus TCN. Therefore, it is demonstrated for the first time in the present study that, by introducing ZIF-8 as an exemplary metal organic framework, transparent porous adsorption layer can be constructed over C_3N_4 photocatalyst without impairing the light absorption ability. Note that, the limited reduction in visible light might be related to the reduced surface defective sites after coating surface ZIF-8 as passivation layer.

Mott-Schottky plots of typical samples were examined to further study their electronic band structures. As shown in Fig. 9b, all the three samples exhibit positive slopes in the Mott-Schottky plots at frequencies of 1, 2, and 3 kHz, which is a typical characteristic of n-type semiconductors. So, their flat band potentials are comparable to the CB potential. And the derived flat-band potential for the sample BCN, TCN, and TCNZ8 is about -1.38, -1.26 and -1.32 V versus Ag/AgCl at pH = 7, respectively. In combination with the bandgap estimated from Fig. 9a, the band alignments for sample BCN, TCN and TCNZ8 are depicted in Fig. S2 (Supporting information). Overall, all these CB values thermodynamically enable photocatalytic CO_2 reduction reactions ($\text{CO}_2/\text{CH}_3\text{OH}$: -0.60 V vs. Ag/AgCl at pH 7). The more negative CB potential of TCNZ8, relative to TCN, makes it thermodynamically stronger for photocatalytic CO_2 reduction reactions. However, owing to a lower flat band potential, TCN possesses a higher electrical conductivity [63], relative to TCNZ8. Therefore, there are both positive and negative

influences from grafted ZIF-8 on the photocatalytic CO_2 reduction performance of $\text{g-C}_3\text{N}_4$ nanotubes.

3.4. Photocatalytic CO_2 reduction activity and processes

Photocatalytic CO_2 reduction with the assistance of water vapor over all the as-prepared samples was measured under the irradiation of a 300 W Xe arc lamp without a UV-cut off filter. Control experiments indicated that no observable hydrocarbon products including CH_4 , HCHO , and HCOOH were detected in the absence of either light irradiation or photocatalysts, suggesting that both light irradiation and photocatalysts are indispensable for CO_2 reduction in the present study.

In this study, in the presence of various as-prepared photocatalyst, CO_2 was generally reduced to methanol (CH_3OH) as the dominant product during the photocatalytic reduction reactions. Methanol is one of the most important chemical products. The *in situ* FTIR spectra were recorded on a typical sample (TCNZ8) to analyze the possible intermediates and the conversion process of photocatalytic CO_2 reduction reaction in the present system. As can be seen from Fig. 10a, the peaks at 1338 , 1504 , and 1620 cm^{-1} are ascribed to carbonate species. Those peaks at 1386 , 1540 , 1568 , 1648 , and 1682 cm^{-1} are attributed to formate species. Two peaks at 1715 and 1429 cm^{-1} are referred to formaldehyde. Another two peaks located at 1732 and 1472 cm^{-1} are derived from the vibration of methoxyl groups [64–66]. According to the existence of different intermediates, the possible mechanism for CH_3OH production can be described using typical two-electron, two-proton reaction pathway ($\text{CO}_2 \rightarrow \text{HCOOH} \rightarrow \text{HCHO} \rightarrow \text{CH}_3\text{OH}$) [5].

As shown in Fig. 10b, it is demonstrated that the photocatalytic activity for CH_3OH production over $\text{g-C}_3\text{N}_4$ photocatalyst can be greatly improved by combined textural and surface guest modification. By solely nanostructural design or ZIF-8 modification, the photocatalytic CH_3OH production activity can be increased by about 90% (Fig. 10). By combined nanostructural design and ZIF-8 modification, the photocatalytic CH_3OH production activity can be increased by more than three times (Fig. 10). Notably, the amount of grafted ZIF-8 nanoclusters is crucial for synergistic nanostructural design and ZIF-8 modification. As illustrated earlier, the surface ZIF-8 grafting significantly promotes the CO_2 capture, which is the very important step before the final surface photocatalytic CO_2 reduction reactions to produce methanol. Usually, higher CO_2 adsorption capacity accompanies with higher photocatalytic CO_2 reduction efficiency for a semiconductor photocatalyst. As a consequence, initially, with increasing amount of grafted ZIF-8 nanoclusters, the photocatalytic CH_3OH production rate of TCNZx continues increasing. However, it seems that the grafted ZIF-8 clusters have bilateral effects on the photocatalytic CH_3OH production properties. In this

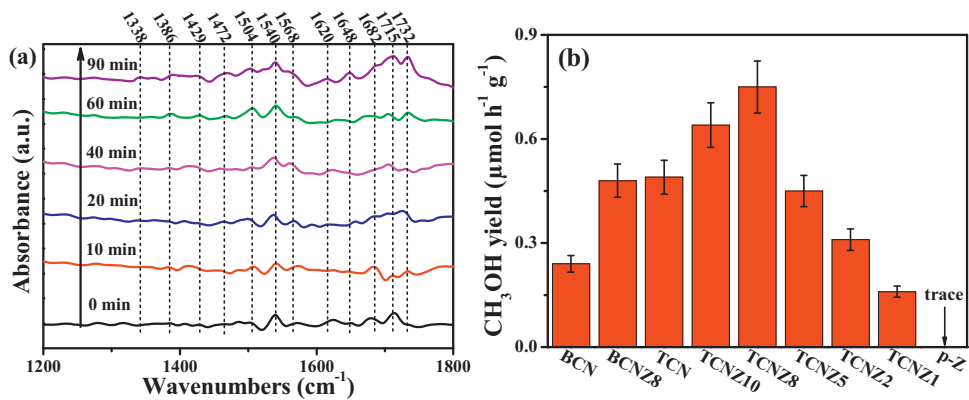


Fig. 10. (a) The *in situ* FTIR spectra of TCNZ8 in a flow of $\text{CO}_2/\text{H}_2\text{O}$ vapour mixture as a function of irradiation time; (b) Comparison of CH_3OH generation rate for the as-prepared samples.

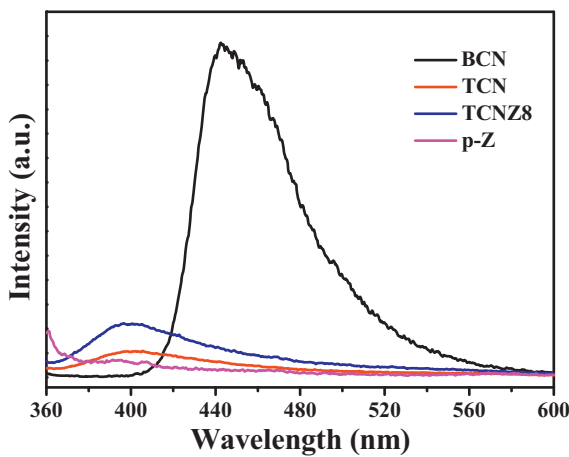


Fig. 11. The steady-state PL spectra of typical samples.

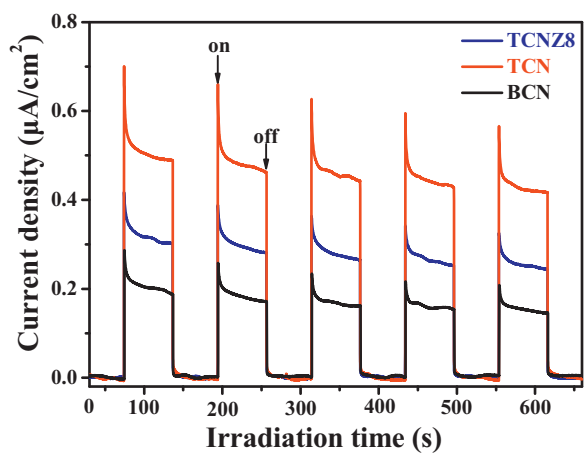


Fig. 12. Transient photocurrent responses for the BCN, TCN, and TCNZ8 samples.

study, as the mass ratio of grafted ZIF-8 clusters to $\text{g-C}_3\text{N}_4$ micro-tubes is 1:8 (that is, sample TCNZ8), the photocatalytic CH_3OH production rate is highest, reaching $0.75 \mu\text{mol h}^{-1} \text{g}^{-1}$. While CO_2 adsorption can be enhanced by surface grafting ZIF-8, the surface charge transfer might be inhibited by the introduced ZIF-8 at the same time, due to the weaker electrical conductivity of ZIF-8. Such an assumption is confirmed by combined analyses of the steady-state photoluminescence (PL) spectra and transient photocurrent responses.

Steady-state PL spectra of the typical as-prepared samples were shown in Fig. 11. While sample BCN showed a strong PL emission peak at about 450 nm, the emission peak of sample TCN shifted to 400 nm because of quantum confinement effects of the unique nanostructure. Meanwhile, the PL intensity of TCN was significantly lower than that of BCN, indicating a much lower recombination rate of charge carriers and a faster charge transfer within the sample TCN, relative to sample BCN. This result strongly suggested that the unique tubular nanostructure facilitated the charge separation efficiency. Unfortunately, after grafting ZIF-8 nanoclusters on the surface of TCN, the PL intensity of TCNZ8 was slightly enhanced. In this regard, the charge separation and transfer efficiency was retarded after surface grafting ZIF-8. Such a conclusion was further confirmed by the photoelectrochemical measurements. As shown in Fig. 12, the transient photocurrent curves for all the three tested samples exhibited an anodic photocurrent spike at the very initial time of light irradiation, and then photocurrent decreases continuously until a constant photocurrent is reached. The photocurrent decay indicates that the holes accumulated at

the surface of $\text{g-C}_3\text{N}_4$ photocatalysts competitively recombine with the electrons from the conduction band, instead of being trapped or captured by reduced species in the electrolyte [54]. The photocurrent becomes constant after the equilibration of competitive separation and recombination of electron-hole pairs. Clearly, the stable photocurrent value for sample TCN was the highest among the three samples, suggesting its fastest charge separation efficiency, which was consistent with the aforementioned PL study. Unfortunately, the surface grafting of ZIF-8 nanoclusters somewhat retarded the charge separation, with consequence of reduced photocurrent intensity for sample TCNZ8, relative to that for pristine TCN. Even though, it was worth mentioning that the photocurrent intensity of sample TCNZ8 was still much higher than the sample BCN.

In this study, it is significantly demonstrated that, a reasonable combination of the nanostructural design and surface modification of $\text{g-C}_3\text{N}_4$ photocatalyst leads to synergistic tuning of the complex interconnected photocatalytic processes, and therefore, the photocatalytic CO_2 reduction ability can be largely improved. First of all, the nanostructural design of $\text{g-C}_3\text{N}_4$ photocatalyst gives rise to unique nanotubes, bringing about significant modification of the optical absorption properties, photocatalytic redox ability and charge separation efficiency. Nevertheless, upon sole nanostructural design, the CO_2 capture capacity is still not satisfying. In this regard, a cooperative surface modification by ZIF-8 grafting is combined to build transparent porous adsorption antenna. As expected, the CO_2 capture capacity can be greatly increased. More significantly, the side effects of adsorption layers in interfering the optical

absorption and charge transfer can be minimized by controlling the loading amount of grafted ZIF-8. As a result, the apparent photocatalytic CO₂ efficiency can be optimized accordingly.

4. Conclusion

In summary, we have successfully synthesized TCN/ZIF-8 composite by growing ZIF-8 nanoclusters on the surface of the preformed g-C₃N₄ nanotubes. The designed hybrid structures not only largely inherited the broadened optical absorption properties, enhanced photocatalytic redox ability and promoted charge separation efficiency from the g-C₃N₄ nanotubes, but also possessed the excellent CO₂ adsorption capacity because of grafting additional ZIF-8 nanoclusters. As a result, the TCN/ZIF-8 composite photocatalyst exhibited a much higher photocatalytic activity for the CO₂ reduction, reaching 0.75 μmol h⁻¹ g⁻¹ under mild reaction condition. This work will enlighten a promising strategy to construct efficient photocatalyst for greenhouse gas CO₂ resourcing, by taking advantage of the cooperative effects of semiconductor nanostructures and surface metal-organic framework grafters. Meanwhile, we noticed that the conductivity of most MOF materials is not good enough, and thus the charge transfer within the photocatalytic system of MOF based composites will be more or less impaired. There is a trade off between the charge transfer and the CO₂ capture in most MOF based composite photocatalysts, and therefore, the loading amount of MOF is always crucial in optimizing the apparent photocatalytic performance.

Acknowledgements

This study is financially supported by NSFC (51572209), the National Key Research and Development Program (2016YFC0204800), the Start-up Funds for High-Level Talents of Sun Yat-sen University (38000-31131103) and the Fundamental Research Funds for the Central Universities (No. 16lgjc64).

Appendix A. Supplementary data

Supplementary data associated with this article can be found, in the online version, at <http://dx.doi.org/10.1016/j.apcatb.2017.04.009>.

References

- [1] S. Cao, J. Low, J. Yu, M. Jaroniec, *Adv. Mater.* 27 (2015) 2150–2176.
- [2] M. Marszewski, S. Cao, J. Yu, M. Jaroniec, *Mater. Horiz.* 2 (2015) 261–278.
- [3] J. Low, J. Yu, W. Ho, *J. Phys. Chem. Lett.* 6 (2015) 4244–4251.
- [4] L. Yuan, Y.J. Xu, *Appl. Surf. Sci.* 342 (2015) 154–167.
- [5] X. Li, J. Wen, J. Low, Y. Fang, J. Yu, *Sci. China Mater.* 57 (2014) 70–100.
- [6] T. Inoue, A. Fujishima, S. Konishi, K. Honda, *Nature* 277 (1979) 637–638.
- [7] L. Liu, H. Zhao, J.M. Andino, Y. Li, *ACS Catal.* 2 (2012) 1817–1828.
- [8] J. Fu, S. Cao, J. Yu, J. Low, Y. Lei, *Dalton Trans.* 43 (2014) 9158–9165.
- [9] Y. He, Y. Wang, L. Zhang, B. Teng, M. Fan, *Appl. Catal. B: Environ.* 168–169 (2015) 1–8.
- [10] J. Jin, J. Yu, D. Guo, C. Cui, W. Ho, *Small* 11 (2015) 5262–5271.
- [11] S. Liu, J. Xia, J. Yu, *ACS Appl. Mater. Interfaces* 7 (2015) 8166–8175.
- [12] J. Low, B. Cheng, J. Yu, *Appl. Surf. Sci.* 392 (2017) 658–686.
- [13] K. Wang, Q. Li, B. Liu, B. Cheng, W. Ho, J. Yu, *Appl. Catal. B: Environ.* 176–177 (2015) 44–52.
- [14] Y. Wang, Y. Xu, Y. Wang, H. Qin, X. Li, Y. Zuo, S. Kang, L. Cui, *Catal. Commun.* 74 (2016) 75–79.
- [15] S. Cao, J. Yu, *J. Phys. Chem. Lett.* 5 (2014) 2101–2107.
- [16] Y. He, L. Zhang, M. Fan, X. Wang, M.L. Walbridge, Q. Nong, Y. Wu, L. Zhao, *Sol. Energy Mater. Sol. C* 137 (2015) 175–184.
- [17] S. Zhou, Y. Liu, J. Li, Y. Wang, G. Jiang, Z. Zhao, D. Wang, A. Duan, J. Liu, Y. Wei, *Appl. Catal. B: Environ.* 158–159 (2014) 20–29.
- [18] J.C. Wang, H.C. Yao, Z.Y. Fan, L. Zhang, J.S. Wang, S.Q. Zang, Z.J. Li, *ACS Appl. Mater. Interfaces* 8 (2016) 3765–3775.
- [19] Z. Yang, X. Xu, X. Liang, C. Lei, Y. Cui, W. Wu, Y. Yang, Z. Zhang, Z. Lei, *Appl. Catal. B: Environ.* 205 (2017) 42–54.
- [20] J. Mao, T. Peng, X. Zhang, K. Li, L. Ye, L. Zan, *Catal. Sci. Technol.* 3 (2013) 1253.
- [21] Y. Wang, F. Wang, Y. Zuo, X. Zhang, L.F. Cui, *Mater. Lett.* 136 (2014) 271–273.
- [22] W.J. Ong, L.L. Tan, S.P. Chai, S.T. Yong, *Chem. Commun.* 51 (2015) 858–861.
- [23] F. Raziq, Y. Qu, X. Zhang, M. Humayun, J. Wu, A. Zada, H. Yu, X. Sun, L. Jing, J. *Phys. Chem. C* 120 (2016) 98–107.
- [24] S.W. Cao, X.F. Liu, Y.-P. Yuan, Z.Y. Zhang, Y.S. Liao, J. Fang, S.C.J. Loo, T.C. Sum, C. Xue, *Appl. Catal. B: Environ.* 147 (2014) 940–946.
- [25] Y. He, L. Zhang, B. Teng, M. Fan, *Environ. Sci. Technol.* 49 (2015) 649–656.
- [26] H. Shi, G. Chen, C. Zhang, Z. Zou, *ACS Catal.* 4 (2014) 3637–3643.
- [27] M. Li, L. Zhang, X. Fan, M. Wu, M. Wang, R. Cheng, L. Zhang, H. Yao, J. Shi, *Appl. Catal. B: Environ.* 201 (2017) 629–635.
- [28] W.J. Ong, L.K. Putri, L.L. Tan, S.P. Chai, S.T. Yong, *Appl. Catal. B: Environ.* 180 (2016) 530–543.
- [29] M. Li, L. Zhang, X. Fan, Y. Zhou, M. Wu, J. Shi, *J. Mater. Chem. A* 3 (2015) 5189–5196.
- [30] W. Yu, D. Xu, T. Peng, *J. Mater. Chem. A* 3 (2015) 19936–19947.
- [31] J. Wen, J. Xie, X. Chen, X. Li, *Appl. Surf. Sci.* 391 (2017) 72–123.
- [32] T. Zhang, W. Lin, *Chem. Soc. Rev.* 43 (2014) 5982–5993.
- [33] J. Yao, H. Wang, *Chem. Soc. Rev.* 43 (2014) 4470–4493.
- [34] S. Liu, J. Wang, J. Yu, *RSC Adv.* 6 (2016) 59998–60006.
- [35] S. Hwang, W.S. Chi, S.J. Lee, S.H. Im, J.H. Kim, J. Kim, *J. Membr. Sci.* 480 (2015) 11–19.
- [36] Z.Y. Yeo, P.Y. Tan, S.P. Chai, P.W. Zhu, A.R. Mohamed, *RSC Adv.* 4 (2014) 52461–52466.
- [37] P. Hu, Y. Yang, Y. Mao, J. Li, W. Cao, Y. Ying, Y. Liu, J. Lei, X. Peng, *CrystEngComm* 17 (2015) 1576–1582.
- [38] J. Gao, Y. Zhou, Z. Li, S. Yan, N. Wang, Z. Zou, *Nanoscale* 4 (2012) 3687–3692.
- [39] B. Zhu, P. Xia, W. Ho, J. Yu, *Appl. Surf. Sci.* 344 (2015) 188–195.
- [40] J. Cravillon, R. Nayak, S. Springer, A. Feldhoff, K. Huber, M. Wiebcke, *Chem. Mater.* 23 (2011) 2130–2141.
- [41] X. Wang, K. Maeda, A. Thomas, K. Takanabe, G. Xin, J.M. Carlsson, K. Domen, M. Antonietti, *Nat. Mater.* 8 (2009) 76–80.
- [42] H. Zheng, Y. Zhang, L. Liu, W. Wan, P. Guo, A.M. Nystrom, X. Zou, *J. Am. Chem. Soc.* 138 (2016) 962–968.
- [43] P.F. Xia, B.C. Zhu, J.G. Yu, S.W. Cao, M. Jaroniec, *J. Mater. Chem. A* 5 (2017) 3230–3238.
- [44] Y. Zheng, L.H. Lin, B. Wang, X.C. Wang, *Angew. Chem. Int. Ed.* 54 (2015) 12868–12884.
- [45] J. Xu, L.W. Zhang, R. Shi, Y.F. Zhu, *J. Mater. Chem. A* 1 (2013) 14766–14772.
- [46] H. Chen, L. Wang, J. Yang, R.T. Yang, *J. Phys. Chem. C* 117 (2013) 7565–7576.
- [47] F. Tian, A.M. Cerro, A.M. Mosier, H.K. Wayment-Steele, R.S. Shine, A. Park, E.R. Webster, L.E. Johnson, M.S. Johal, L. Benz, *J. Phys. Chem. C* 118 (2014) 14449–14456.
- [48] J. Zhang, M. Zhang, G. Zhang, X. Wang, *ACS Catal.* 2 (2012) 940–948.
- [49] Q. Han, B. Wang, J. Gao, Z. Cheng, Y. Zhao, Z. Zhang, L. Qu, *ACS Nano* 10 (2016) 2745–2751.
- [50] Q. Liang, Z. Li, Z.H. Huang, F. Kang, Q.H. Yang, *Adv. Funct. Mater.* 25 (2015) 6885–6892.
- [51] X. Bai, J. Li, C. Cao, *Appl. Surf. Sci.* 256 (2010) 2327–2331.
- [52] M. Tahir, C. Cao, F.K. Butt, S. Butt, F. Idrees, Z. Ali, I. Aslam, M. Tanveer, A. Mahmood, N. Mahmood, *CrystEngComm* 16 (2014) 1825.
- [53] S.C. Yan, Z.S. Li, Z.G. Zou, *Langmuir* 25 (2009) 10397–10401.
- [54] Q. Xiang, J. Yu, M. Jaroniec, *J. Phys. Chem. C* 115 (2011) 7355–7363.
- [55] S. Wang, C. Li, T. Wang, P. Zhang, A. Li, J. Gong, *J. Mater. Chem. A* 2 (2014) 2885.
- [56] L. Lin, T. Zhang, H. Liu, J. Qiu, X. Zhang, *Nanoscale* 7 (2015) 7615–7623.
- [57] K.S.W. Sing, D.H. Everett, R.A.W. Haul, L. Moscou, R.A. Pierotti, J. Rouquerol, T. Siemieniewska, *Pure Appl. Chem.* 57 (1985) 603–619.
- [58] J. Yu, S. Wang, B. Cheng, Z. Lin, F. Huang, *Catal. Sci. Technol.* 3 (2013) 1782.
- [59] J. Yu, S. Wang, J. Low, W. Xiao, *Phys. Chem. Chem. Phys.* 15 (2013) 16883–16890.
- [60] Q. Huang, J. Yu, S. Cao, C. Cui, B. Cheng, *Appl. Surf. Sci.* 358 (2015) 350–355.
- [61] M. Tahir, C. Cao, F.K. Butt, F. Idrees, N. Mahmood, Z. Ali, I. Aslam, M. Tanveer, M. Rizwan, T. Mahmood, *J. Mater. Chem. A* 1 (2013) 13949.
- [62] D. Esken, H. Noei, Y. Wang, C. Wiktor, S. Turner, G. Van Tendeloo, R.A. Fischer, *J. Mater. Chem.* 21 (2011) 5907.
- [63] S. Yang, Y. Gong, J. Zhang, L. Zhan, L. Ma, Z. Fang, R. Vajtai, X. Wang, P.M. Ajayan, *Adv. Mater.* 25 (2013) 2452–2456.
- [64] J. Fu, B. Zhu, C. Jiang, B. Cheng, W. You, J. Yu, *Small* (2017), <http://dx.doi.org/10.1002/smll.201603938> (1–9).
- [65] W. Wang, D. Xu, B. Cheng, J. Yu, C. Jiang, *J. Mater. Chem. A* 5 (2017) 5020–5029.
- [66] J. Wang, P. Zhang, J. Li, C. Jiang, R. Yunus, J. Kim, *Environ. Sci. Technol.* 49 (2015) 12372–12379.